

JGR Solid Earth

RESEARCH ARTICLE

10.1029/2019JB018377

Key Points:

- Stress inversion reveals stress heterogeneity and a gradual transition from strike-slip to oblique normal faulting in Oklahoma
- Most but not all reactivated faults are optimally oriented in the present-day stress field in Oklahoma
- Comparison of reactivated faults, basement fractures, and mapped sedimentary faults suggests common tectonic control

Supporting Information:

- Supporting Information S1
- Data Set S1
- Data Set S2

Correspondence to:

Y. Qin,
 Yan.Qin-1@ou.edu

Citation:

Qin, Y., Chen, X., Walter, J. I., Haffener, J., Trugman, D. T., Carpenter, B. M., et al. (2019). Deciphering the stress state of seismogenic faults in Oklahoma and southern Kansas based on an improved stress map. *Journal Geophysical Research: Solid Earth*, 124, 12,920–12,934. <https://doi.org/10.1029/2019JB018377>

Received 12 JUL 2019

Accepted 13 NOV 2019

Accepted article online 23 NOV 2019

Published online 4 DEC 2019

©2019. American Geophysical Union.
 All Rights Reserved.

Deciphering the Stress State of Seismogenic Faults in Oklahoma and Southern Kansas Based on an Improved Stress Map

Yan Qin¹ , Xiaowei Chen¹ , Jacob I. Walter² , Jackson Haffener¹, Daniel T. Trugman³ , Brett M. Carpenter¹ , Matthew Weingarten⁴ , and Folarin Kolawole¹ 

¹School of Geosciences, University of Oklahoma, Norman, OK, USA, ²Oklahoma Geological Survey, University of Oklahoma, Norman, OK, USA, ³Earth and Environmental Sciences Division – Geophysics Group, Los Alamos National Laboratory, Los Alamos, NM, USA, ⁴Department of Geological Sciences, San Diego State University, San Diego, CA, USA

Abstract Fault location and geometry are critical considerations in the reactivation of preexisting faults. Here, we combine relocated earthquake catalogs and focal mechanisms to delineate seismogenic faults in Oklahoma and southern Kansas and analyze their stress state. We first identify and map seismogenic faults based on earthquake clustering. We then obtain an improved stress map using 2,047 high-quality focal mechanisms. The regional stress map shows a gradual transition from oblique normal faulting in western Oklahoma to strike-slip faulting in central and eastern Oklahoma. Stress amplitude ratio shows a strong correlation with pore pressure from hydrogeologic models, suggesting that pore pressure exhibits a measurable influence on stress patterns. Finally, we assess fault stress state via 3-D Mohr circles; a parameter *understress* is used to quantify the level of fault criticality (with 0 meaning critically stressed faults and 1 meaning faults with no applied shear stress). Our results indicate that most active faults have near vertical planes (planarity >0.8 and dip >70°), and there is a strong correlation between fault length and maximum magnitude on each fault. The fault trends show prominent conjugate sets that strike [55–75°] and [105–125°]. A comparison with mapped sedimentary faults and basement fractures reveals common tectonic control. Based on 3-D Mohr circles, we find that 78% of the faults are critically stressed (*understress* ≤0.2), while several seismogenic faults are misoriented with high *understress* (>0.4). Fault geometry and local stress fields may be used to evaluate potential seismic hazard, as the largest earthquakes tend to occur on long, critically stressed faults.

1. Introduction

The recent increase in seismicity in Oklahoma has been associated with wastewater injection (e.g., Ellsworth, 2013; Keranen et al., 2014; Yeck et al., 2016). The basic mechanism driving this seismicity is well established: Increased pore pressure in the fault zone will lead to a reduction in the effective normal stress on the fault, thereby reducing fault strength and promoting fault slip (e.g., Healy et al., 1968; King Hubbert & Rubey, 1959; Raleigh et al., 1976). Based on this mechanism, the orientation of the faults and the regional stress field are crucial to assess the likelihood of reactivation. Faults that are optimally oriented with respect to the regional stress field will be readily reactivated, while faults that are nonoptimally oriented will require a much larger pore pressure increase to slip. Holland (2013) and Darold and Holland (2015) tried to differentiate optimally oriented faults from nonoptimally oriented faults based on probability density functions of fault strikes relative to a uniform maximum horizontal compressional stress orientation of N85° E. Alt and Zoback (2017) analyzed regional stress fields for Texas, Oklahoma, and Kansas combining stress inversions from focal mechanism solutions and wellbore measurements. Walsh and Zoback (2016) simulated the conditional probability of fault slip related to injection-induced earthquakes by incorporating the uncertainty of the stress tensor, pore pressure, friction coefficient, and fault orientation.

While previous studies have provided overall knowledge of the ambient stress field in Oklahoma and southern Kansas, a high-resolution stress map is needed to systematically assess fault criticality under the local stress field. This is especially important with the growing evidence that poroelastic stress (e.g., Barbour et al., 2017; Deng et al., 2016; Goebel et al., 2017; Segall & Lu, 2015) and aseismic creep propagation (e.g., Cappa et al., 2019; Eyre et al., 2019) could, in part, drive some of the induced seismicity. In this study, we develop a

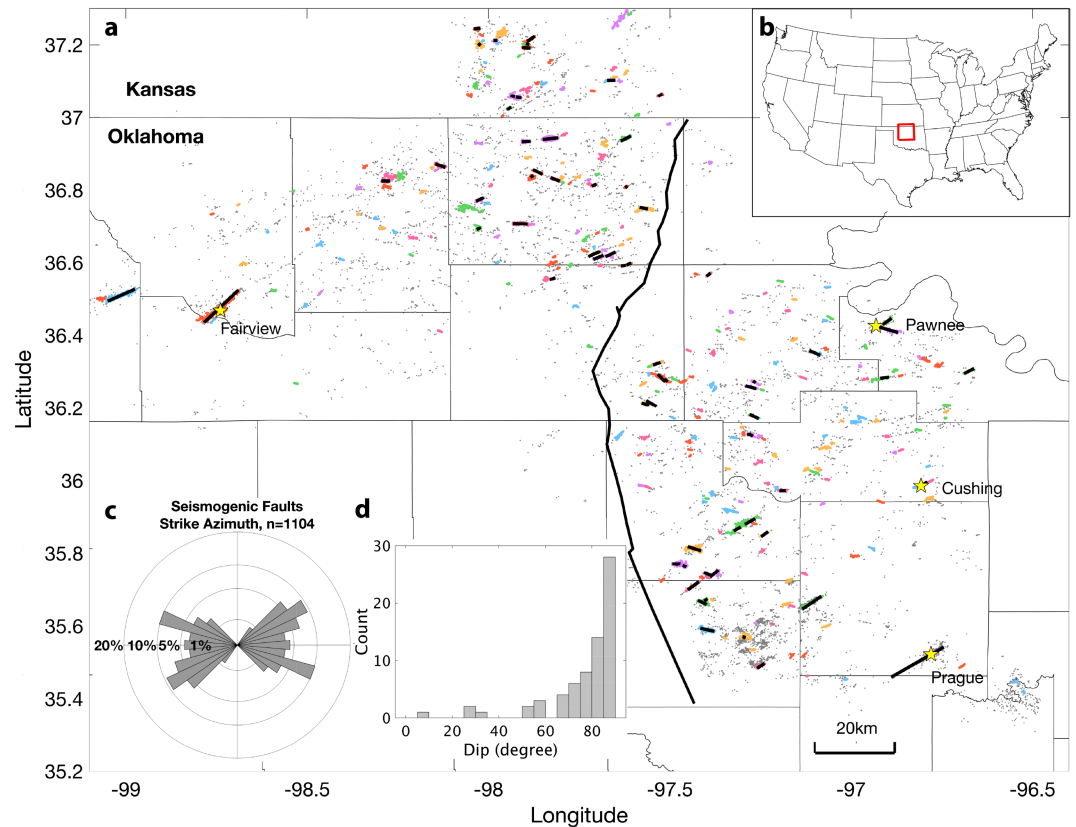


Figure 1. Mapped faults in this study based on earthquake relocations from Chen (2016) and Schoenball and Ellsworth (2017a). (a) Earthquake clusters (colored dots) with 10 and more events. Short, black lines show the faults with planarity larger than 0.8 mapped from 30 and more events. Yellow stars show the location of four $M \geq 5$ earthquakes in Oklahoma. Thin, black lines are county boundaries in Oklahoma. The long, thick black line is the Nemaha fault from OGS fault database (Marsh & Holland, 2016). (b) The inset map shows the location of the study area. (c) Histogram of strike of faults in (a). (d) Histogram of dip of faults in (a).

stress map with relatively high spatial resolution using a suite of 2,047 focal mechanism solutions obtained from Oklahoma and southern Kansas, allowing for more precise quantitative analysis of the fault stress state.

For a given background stress field, a complete knowledge of the preexisting fault system is critical to evaluate the induced earthquake hazard (Levandowski et al., 2018a; Yeck et al., 2016). Oklahoma and southern Kansas are located in the Precambrian (~ 1.4 Ga) Southern Granite-Rhyolite Province of the Mid-Continent U.S. craton (Denison et al., 1987). This granitic basement hosts most of the current seismicity (Schoenball & Ellsworth, 2017a; Kolawole, Johnston, et al., 2019). This basement is characterized by a structural fabric with dominant discontinuity zones that trend NW-SE, NE-SW, and a minor N-S set (Kolawole, Johnston, et al., 2019). This structural fabric resulted from the multiphase Proterozoic contractional and extensional deformation events that affected the central United States, for example, development of Granite-Rhyolite Provinces and the Mid-Continent Rift (Bickford et al., 2015; Whitmeyer & Karlstrom, 2007). The fault database of Oklahoma (Marsh & Holland, 2016) shows several fault segments and large (> 50 -km-long) \sim N-S trending faults within the north-central region. Recent 3-D seismic data (Chopra et al., 2018; Kolawole, Carpenter, et al., 2019; Liao et al., 2017) reveal that these large N-S faults and the associated secondary splays are basement rooted. The Oklahoma Geological Survey (OGS) fault database (Marsh & Holland, 2016) largely contains sedimentary faults that represent (1) reactivation and propagation of the Precambrian basement structural trends (NW, NE, and N-S) into the sedimentary cover (Kolawole, Carpenter, et al., 2019) and (2) additional deformation by the development of pervasive R-shears that splay outward from the major right-lateral N-S faults (Chopra et al., 2018; Kolawole, Carpenter, et al., 2019; Liao et al., 2017).

The majority of earthquakes in Oklahoma do not occur on currently mapped faults in the OGS database (e.g., Alt & Zoback, 2017; Goebel et al., 2017; Keranen et al., 2013; Yeck et al., 2016). The linear trends of

seismicity (Figure 1) suggest that most earthquakes occur on basement faults that are likely unmapped in the current fault database (Schoenball & Ellsworth, 2017b; Skoumal et al., 2019). Several studies have used the spatial distribution of seismicity to map fault segments in Oklahoma. For example, splays of the Wilzetta fault were mapped from 2011 Mw5.7 Prague earthquake sequence (Keranen et al., 2013); the extension of a mapped fault segment was delineated from the 2016 Mw5.1 Fairview earthquake sequence (Yeck et al., 2016); and the Sooner Lake Fault as the conjugate fault of the mapped Labette Fault was mapped from 2016 Mw5.8 Pawnee earthquake sequence (Chen et al., 2017).

In this study, we systematically map the reactivated faults (herein referred to as seismogenic faults) and analyze the fault criticality within an improved knowledge of the local stress field. First, we characterize the geometry of seismogenic faults in Oklahoma and southern Kansas based on earthquake clustering. Second, we use a high-quality catalog of focal mechanism solutions to perform a detailed stress inversion. Then we assess the stress state of individual faults with in situ 3-D Mohr circles and evaluate the influence of fault criticality on fault reactivation. Finally, we compare seismogenic faults with mapped sedimentary faults from different subregions in Oklahoma and fracture systems in outcrops of the seismogenic basement. Moreover, the stress field and fault stress state are compared with pore pressure from hydrogeologic models to further understand the influence of wastewater injection on fault reactivations. These results help to provide a comprehensive understanding of the roles of preexisting faulting, fluid injection, and stress state in fault reactivation and potential earthquake hazard.

2. Data

High-precision earthquake relocations can reveal tightly clustered seismicity patterns and help identify in situ fault locations and orientations. In this study, we use the relocated catalog from Chen (2016) for pre-2013 events and Schoenball and Ellsworth (2017a) for later events to map seismogenic faults. The catalog in Chen (2016) uses a 3-D velocity model and the double-difference method (Waldhauser, 2001) with catalog differential times to relocate earthquakes. The catalog in Schoenball and Ellsworth (2017a) uses a 1-D velocity model and the double-difference method with differential times derived from waveform cross correlation to relocate earthquakes from 2013 to 2017 and has high relative location precision (50 m horizontally and 200 m vertically) with the inclusion of industry networks and higher precision of differential times. The magnitude of completeness for catalogs from Chen (2016) and Schoenball and Ellsworth (2017a) is 2.7 and 2.8, respectively. We verify that for 13,512 common earthquakes from Chen (2016) and Schoenball and Ellsworth (2017a), the median location difference is 0.42 km (Figure S1 in the supporting information), which mainly comes from some systematical shift of absolute locations due to the difference in velocity model but does not affect relative locations within clusters. We use Chen (2016) catalog mainly for the Prague fault with M5.7 earthquake in 2011. Other pre-2013 faults from Chen (2016) do not meet the minimum number requirement of 30 and are not included.

For focal mechanism solutions in Oklahoma, we select 1,823 focal mechanism solutions of A and B quality in the catalog provided by OGS (Sylvester, 1988) from January 2010 to August 2018, which are computed via HASH (Hardebeck & Shearer, 2008) program with at least eight routinely picked first motion polarities. The selected focal mechanism solutions have an average RMS fault plane uncertainty less than 35° and a station distribution ratio larger than 0.4. For southern Kansas, we apply the same criteria and compute 224 A and B quality focal mechanism solutions using the first motion polarities in the HASH program. The focal mechanism solutions in southern Kansas are consistent with Rubinstein et al. (2018). In total, we have 2,047 focal mechanism solutions for stress inversion.

3. Methods

3.1. Clustering and Fault Mapping

We use a hierarchical clustering program in MATLAB to cluster the earthquakes based on the epicenter of the relocations. In this method, the events are linked based on the nearest distance between each event pair, and a distance cutoff of 0.46 km is selected by trail and error to group events with distance smaller than the cutoff into a cluster. The program identifies 84 clusters with more than 30 events (Figure 1). The clustering results show similar fault trends as in Schoenball and Ellsworth (2017b) from a different clustering method. We use a relatively longer distance cutoff in the clustering process, and some clusters include several trends of events close to each other, which are then separated manually to calculate the fault geometries.

For each cluster and some manually separated subclusters with 30 or more events, we use principal component analysis (Vidale & Shearer, 2006) to fit a fault plane. First, a 3×3 covariance matrix D from the earthquake hypocenters is calculated, and the eigenvalues ($\lambda_1 \geq \lambda_2 \geq \lambda_3$) and the corresponding eigenvectors U_1 , U_2 , and U_3 of D define the principal axes of rotational inertia for the points in each cluster. The first two eigenvectors U_1 and U_2 represent the surface of the fault plane, and U_3 is normal to the fault plane. The fault strike and dip angle are calculated from the direction of the normal vector U_3 . The planarity of seismicity hypocenters is defined as $1 - \lambda_3/\lambda_2$ (Vidale & Shearer, 2006). At its extremes, a planarity of 1 indicates a perfectly planar shape, and a planarity of 0 indicates a nearly spherical cloud of seismicity (Vidale & Shearer, 2006). Of the 95 planarity values 69 (73%) are larger than 0.8, suggesting most clusters occur on well-defined fault plane. Since most of the seismogenic faults can be fit with a fault plane, the fault length is estimated manually based on the seismicity extension along the axis of the largest eigenvector.

3.2. Stress Inversion Method

To obtain a detailed in situ stress field, we use the MSATSI software package (Martínez-Garzón et al., 2014) to invert the stress field from earthquake focal mechanism solutions. The MSATSI software is a MATLAB wrapper of the SATSI (Hardebeck & Michael, 2006) based on the inversion from Michael (1984). The inversion relies on three assumptions: (1) The stress field is homogeneous over the spatial and temporal extent of the events in each grid; (2) the focal mechanism solutions are adequately diverse, such as the RMS angular difference from the average mechanism in each grid of at least $\sim 40\text{--}45^\circ$ (Hardebeck & Hauksson, 2001) to constrain the solution; and (3) seismic slip occurs in the direction of the resolved shear traction acting on preexisting faults. With 2,047 focal mechanism solutions for Oklahoma and southern Kansas, the study area is first gridded with 0.4° by 0.4° , and if 100 or more events are in one grid, the grid is then subdivided into two or four evenly spaced subgrids in latitude and longitude as long as there are still more than 50 events in each subgrid. This method covers as much area as possible in the inversion and ensures adequate variety to constrain the solution (Martínez-Garzón et al., 2016a) in each grid. As a result, the study area is separated into 24 grids, and a damped inversion is performed on those grids. A map with the number of focal mechanisms in each grid is shown in Figure S2. The inversion results include the orientations of the three principal stress axes and a measure of their relative amplitudes R ,

$$R = \frac{\sigma_1 - \sigma_2}{\sigma_1 - \sigma_3}, \quad (1)$$

where σ_1 , σ_2 , and σ_3 are the maximum, intermediate, and minimum principal stresses, respectively. The uncertainties of the inversion results are estimated by 1,000 bootstrap resamplings of the focal mechanism solutions associated within each grid.

3.3. Focal Mechanism Tomography

The focal mechanism tomography (FMT) technique was developed to estimate the fluid pore pressure field from earthquake focal mechanism solutions under a given stress field (Terakawa et al., 2010). In this study, we adopt the assumptions in Terakawa et al. (2010) to convert the relative stress amplitude to a 3-D stress tensor and use the local stress tensor to evaluate the stress state of individual faults. The assumptions are as follows: (1) Fault strength is controlled by the Coulomb failure criterion with a constant friction coefficient (Byerlee, 1978), (2) seismic slip occurs in the direction of the resolved shear traction acting on preexisting faults (Wallace, 1951; Bott, 1959), and (3) seismic slip on optimally oriented faults relative to the regional stress pattern occurs under hydrostatic pressure. Based on these assumptions, we have

$$\sigma_1 \left(\sqrt{\mu^2 + 1} - \mu \right) - \sigma_3 \left(\sqrt{\mu^2 + 1} + \mu \right) = 2C - 2\mu P_w, \quad (2)$$

where σ_1 and σ_3 are the maximum and minimum principal stresses, C is the cohesion of fault and assumed as zero in the following calculation, P_w is the hydrostatic pressure at depth, and μ is the friction coefficient without pore pressure influence, assumed to be 0.68 in the analysis. The friction coefficient of 0.68 is based on the average value of lab results of basement rock samples in Oklahoma by Kolawole, Johnston, et al. (2019). The choice of friction coefficient is also consistent with the estimated value of 0.65 using STRESSINVERSE program by Vavryčuk (2014). A sensitivity test of friction coefficient is performed in the discussion section. The derivation of equation (2) is shown in the supporting information.

We further assume that the vertical stress is the weight of overburden,

$$\sigma_v = \rho g z, \quad (3)$$

where ρ is the rock density, $\rho = 2,540 \text{ kg/m}^3$ (Terakawa et al., 2010), g is the acceleration due to gravity, and z is the depth. The stress inversion results show both strike-slip faulting regime and oblique normal faulting regime, so instead of assuming the vertical stress is the intermediate principal stress, it is strictly derived from the principal stress tensor, $\sigma_v = \sigma_v(\sigma_1, \sigma_2, \sigma_3)$ using the orientations of the principal stresses. The derivation is shown in the supporting information.

The ratio of principal stresses from the stress inversion (equation (1)) is also incorporated to solve for the intermediate stress amplitude (Quinones et al., 2018). By solving equations (1)–(3), we can get the stress amplitude for each grid. With the stress tensor known, we compute shear and normal stress on faults, project them onto Mohr circle, and calculate the required pore pressure for fault failure. To project all faults onto the same 3-D Mohr circle, we keep the local stress orientations of each grid and calculate a uniform stress amplitude by averaging over all grids. We will justify the use of uniform stress amplitude by comparing the results from uniform and nonuniform stress field in the discussion. The stress amplitudes and fluid pore pressure calculated from the above assumptions are proportional to the depth (Figure S3). As the catalogs we use have relatively large depth uncertainty, the depth of the mapped faults is not well resolved. We introduce a normalized parameter understress to eliminate the depth dependence of the fault stress state following Gischig (2015):

$$\text{understress} = (\tau_p - \tau_0) / \tau_p, \quad (4)$$

where τ_0 is shear stress on the fault calculated from the fault geometry and stress orientations and τ_p is shear stress at which slip initiates based on the Coulomb failure criterion under hydrostatic pore pressure. Since both τ_0 and τ_p increase linearly with depth, the defined parameter understress is independent of depth. The understress can be used to quantitatively measure fault criticality relative to local stress field. Values of understress near 0 imply that the faults are critically stressed, while values near 1 imply negligible resolved shear stress applied on the fault, and the fault is least favorably oriented. We also calculate the parameter of excess pore pressure, which is defined as the required pore pressure increase above hydrostatic pressure for fault failure according to Mohr circle.

4. Results

4.1. Clustering and Fault Mapping

We identify 84 clusters with 30 or more events and pick 95 fault segments (some clusters are manually separated based on visual inspection). A subset of 69 faults with planarity larger than 0.8 is selected and used in the following analysis (see Figure 1a, Figure S4 and S5 for close-up views of the clusters). The newly mapped faults from several large earthquake sequences are consistent with previous studies (e.g., Keranen et al., 2013; Yeck et al., 2016; Yeck et al., 2017). Specifically, we find that the main fault in Prague is a splay of the Wilzetta fault with an azimuth of 55° and a dip angle of 86° ; the Fairview fault is as an extension of a mapped fault to the southeast; and a conjugate fault pattern is delineated in the Pawnee area. The west-northwest and east-northeast trends of faults in southern Kansas are in agreement with the observations in Rubinstein et al. (2018). Most of the faults in Oklahoma are distributed in the central and northern pressurized regions (Walsh & Zoback, 2016; Skoumal et al., 2019). The distributions of strike and dip angles for these faults are shown in Figures 1c and 1d. The strike angle is mainly distributed in the ranges of $[55\text{--}75^\circ]$ and $[105\text{--}125^\circ]$, which form conjugate patterns relative to a maximum horizontal compression stress orientation of $\text{N}85^\circ\text{E}$. The majority ($>80\%$) of seismogenic faults are steeply dipping with a dip angle larger than 70° . Four faults show dip angle smaller than 35° . Those faults are mapped from fewer than 45 relatively scattered events, so the fault geometries are likely not well constrained.

4.2. Stress Field

Stress inversion provides a stress field with higher spatial resolution compared to previous studies in Oklahoma. Figure 2 shows the map view of maximum horizontal compressive stress (σ_{Hmax}) orientations colored by faulting type. Central Oklahoma is mostly in a strike-slip faulting regime (green bars), whereas north and northwest Oklahoma show a transition from strike-slip to oblique normal faulting regime (black bars). The dominant orientation of σ_{Hmax} is $80\text{--}90^\circ$ (Figure 2b). Those observations are consistent with previous studies (e.g., Levandowski et al., 2018b; Marsh & Holland, 2016; Qi, 2016; Walsh & Zoback, 2016). The stress field in southern Kansas is characterized by strike-slip faulting with σ_{Hmax} of $75\text{--}82^\circ$, which are consistent with Rubinstein et al. (2018).

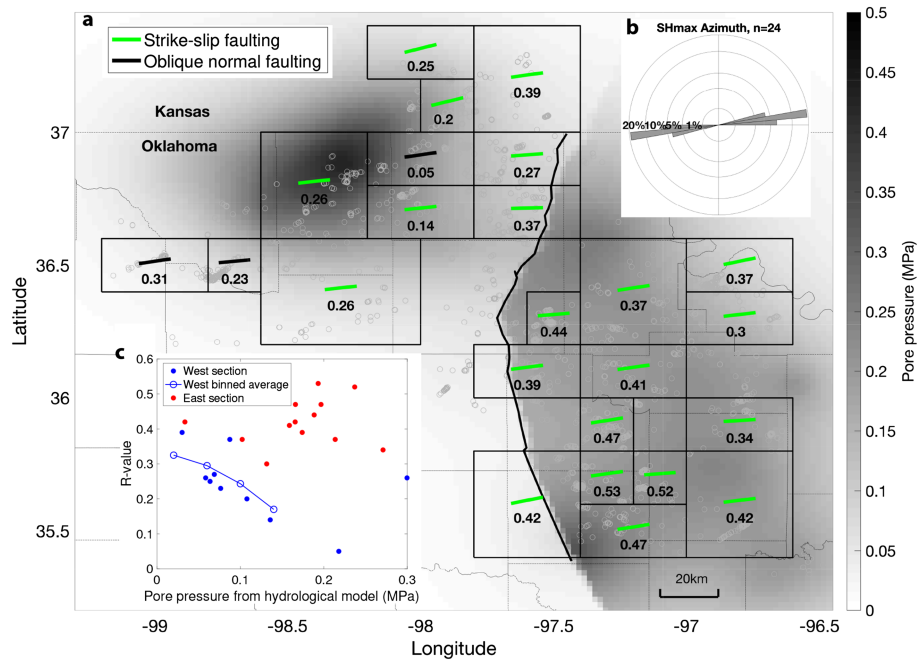


Figure 2. Stress inversion results for Oklahoma and southern Kansas. (a) The bars show the orientation of the maximum horizontal stress (σ_{Hmax}) axis. Green: strike-slip faulting; black: oblique normal faulting. Faulting regime is assigned according to Zoback (1992). The number in the grid shows the corresponding R value. Gray circles are focal mechanisms used in the inversion. Thin, gray lines are county boundaries in Oklahoma. The long, thick black line is the Nemaha fault. (b) Rose diagram of σ_{Hmax} orientation. (c) Cross plot of R value and calculated pore pressure from Langenbruch et al. (2018). The background shows the calculated pore pressure by November 2016 from hydrogeologic models (Langenbruch et al., 2018).

The stress amplitude ratio R also shows spatial variations. The stress field in northern Oklahoma and southern Kansas show smaller R values than other areas, which might indicate the influence of pore pressure. The study area is separated into two major pressure zones using the Nemaha fault as a pressure boundary (Haffener et al., 2018), referred to as the eastern and western pressure zones. We obtain the pore pressure for each grid by averaging pressure values from Langenbruch et al. (2018) at the median occurrence time from all earthquakes within each grid. Using pore pressure values at all grids, we calculate an average R value from all R values within each pressure bin of 0.04 MPa. The result is shown in Figure 2c. For the area west of Nemaha Fault Zone, we obtain negative correlation between R value and pore pressure. A similar

relationship between pore pressure and R value has been observed at Geysers geothermal field (Martínez-Garzón et al., 2016b). However, the eastern Oklahoma region does not show a clear relationship between R value and pore pressure.

The uncertainties of the σ_{Hmax} orientation and R value are estimated from bootstrap resamplings (Figure S6). The highest uncertainty of σ_{Hmax} (defined as one standard deviation) is less than 2° . The uncertainty in the R value is less than 0.05. The inversion results and their small uncertainties suggest that the heterogeneity of the stress field is well constrained using the high-quality focal mechanism solutions.

4.3. Fault Stress State

Using the FMT method, we first calculate the uniform principal stress amplitude gradients as $\sigma_1 = 30.0$ MPa/km, $\sigma_2 = 24.8$ MPa/km, and $\sigma_3 = 15.5$ MPa/km under $\mu = 0.68$. Based on the fault orientation and regional stress field, the shear and normal stress on seismogenic faults are calculated and plotted on 3-D Mohr circle. The understress parameter on each fault is determined by equation (4). As shown in Figure 3, each fault is projected onto a 3-D Mohr circle as a point colored by its understress

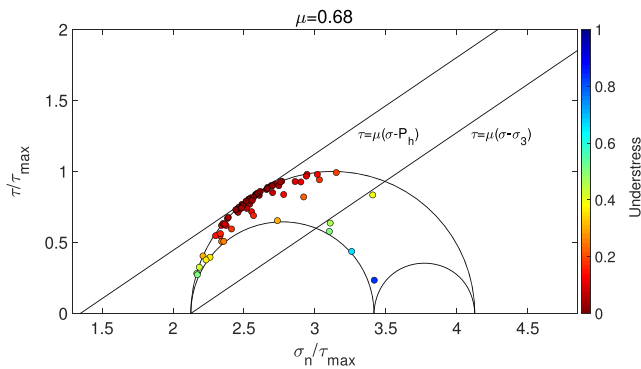


Figure 3. The stress state of 69 seismogenic faults in a 3-D Mohr diagram. The three semicircles represent the stress tensor, and the two straight lines represent the fault strength under hydrostatic fluid pressure and lithostatic pressure under friction coefficient of 0.68. Each circle, colored by understress value, represents the shear and normal stress on a single fault.

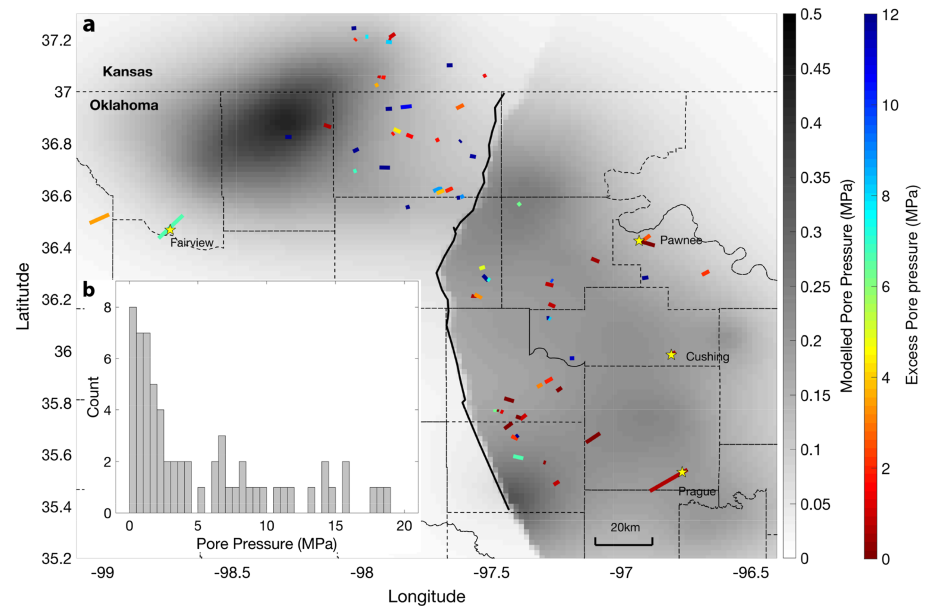


Figure 4. (a) Seismogenic fault map colored by excess pore pressure. Yellow stars show the location of four $M \geq 5$ earthquakes in Oklahoma. The dashed lines are county boundaries. The long, thick black line is the Nemaha fault. The background shows the calculated pore pressure by November 2016 from Langenbruch et al. (2018). (b) Histogram of excess pore pressure on each fault.

value. Most faults (78%) are close to failure limit of the hydrostatic fault strength with understress smaller than 0.2. Four faults with small dip angle $<35^\circ$ show large understress (>0.5). This is possibly due to large uncertainties of the dip angle, and the indication of tensile failure (fluid pressure beyond σ_3) is actually an artifact. Other than that, there are still several nonoptimally oriented faults being reactivated, which might occur at step overs or rotations at different segments of the optimally oriented fault and result from either high pore pressure increase or other factors, for example, static stress change from earthquakes on the main fault.

The required pore pressure to induce failure on each fault is calculated from FMT and shown in Figure 4. The median and mean excess pore pressure (above hydrostatic pore pressure) is 2.7 and 6.9 MPa, respectively under an assumption of fault depth of 5 km. The uniform depth is chosen because the depth of seismogenic faults is not well constrained, and the earthquakes have an average depth of 5 km. The required pore pressure increases are consistent with the estimated pore pressure using similar geomechanical analysis for multiple induced clusters in Texas (Quinones et al., 2018; Snee & Zoback, 2016). The observed pore pressure range is also consistent with the findings in the Geyser geothermal field in Martínez-Garzón et al. (2016c), where faults with a broad range of orientations are activated by fluid injection and the misoriented faults are mostly activated during high injection rates in proximity to the injection wells by an estimated pore pressure increase of ~ 10 MPa.

5. Discussion

5.1. Influence of Pore Pressure on Stress Field and Stress State

In the above analysis, we only consider the pore pressure increase in fault reactivation. The observed negative relationship between R and pore pressure in western pressure zone in Figure 2c could possibly reflect the poroelastic effects by injection. Altmann et al. (2014) gives the analytical solutions to poroelastic equations in 3-D isotropic, homogeneous space. In strike-slip regime along vertical direction, pore pressure increase ΔP induces effective stress amplitude changes of $-\frac{2}{3}\Delta P$, $-\frac{1}{3}\Delta P$, and $-\frac{2}{3}\Delta P$ in σ_1 , σ_2 , and σ_3 orientations, respectively. The pore pressure brings the σ_1 and σ_2 closer and results in a smaller R value. Martínez-Garzón et al. (2013) has observed that stress perturbation due to fluid injection decreases over time with repeated injections. The lack of correlation between R and pore pressure in the eastern section is likely due to the overall higher pore pressure from the longer injection period (e.g., Keranen et al., 2014).

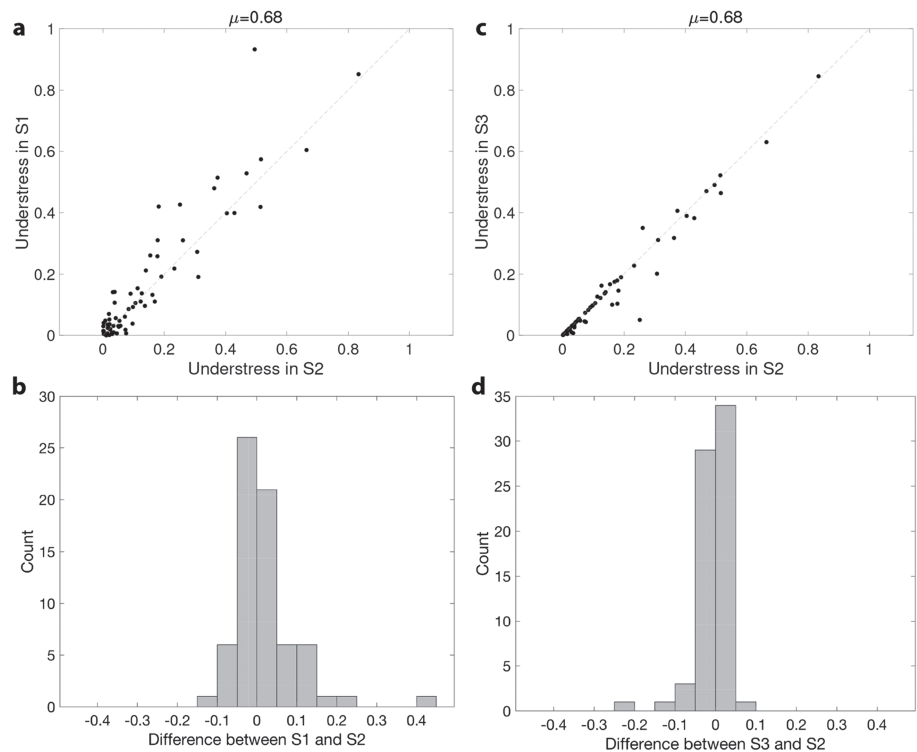


Figure 5. Fault understress values from each stress field scenario. (a) Crossplot of understress values between Scenarios S1 and S2. (b) Histogram of understress difference between Scenarios S1 and S2. (c) Crossplot of understress values between Scenarios S3 and S2. (d) Histogram of understress difference between Scenarios S3 and S2.

To study the relationship between pore pressure and fault reactivation, we compare our results to the modeled pore pressure from Langenbruch et al. (2018). The modeled pore pressure map is overlain by seismogenic faults colored by excess pore pressure computed in this study in Figure 4. As a qualitative first-order observation, the faults that are misoriented and require a relatively larger pore pressure increase are distributed close to the higher pore pressure areas in central and northern Oklahoma. However, scatter plots of understress/excess pore pressure and modeled pore pressure (Figure S7) do not show any significant correlation. We also notice that the pore pressure from Mohr circle analysis is much higher than the pore pressure from hydrogeologic models.

The lack of significant correlation between calculated pore pressure from Mohr's circle and pore pressure from hydrogeologic models in Figure S7 could be due to the uncertainty of fault geometries during excess pore pressure calculation. To account for the uncertainties in fault strike and slip from fault mapping, we add to each fault strike and dip a random uncertainty drawn from a normal distribution with standard deviation of 5° and 10° , respectively. Then the understress is calculated using the new fault strike and dip angle. The procedure is repeated for 200 times. The required mean pore pressure with one standard deviation is shown for each fault in Figure S8. The uncertainty from the strike and dip alone can cause the required pore pressure to change 2 to 12 MPa. We should notice that the original values of required pore pressure fall within the uncertainty test.

The lack of correlation in Figure S7 can also be due to heterogeneity in subsurface hydrogeologic parameters that is not considered in the pore pressure model in Langenbruch et al. (2018). Permeability heterogeneity has been shown to be lognormally distributed in space, and therefore, certain localized regions may have locally higher pore pressure perturbations than the larger regional pore pressure perturbation. As an example, Chen et al. (2018) demonstrated that a highly permeable fault damage zone could significantly enhance the pore pressure within the fault zone compared to isotropic hydrological structure. These factors likely prevent a strong correlation for individual fault parameters. On the other hand, the stress tensor is derived from events distributed within a larger grid (i.e., much larger than individual events) and represents the averaged effect of regional pore pressure variations, so we cannot see a stronger correlation.

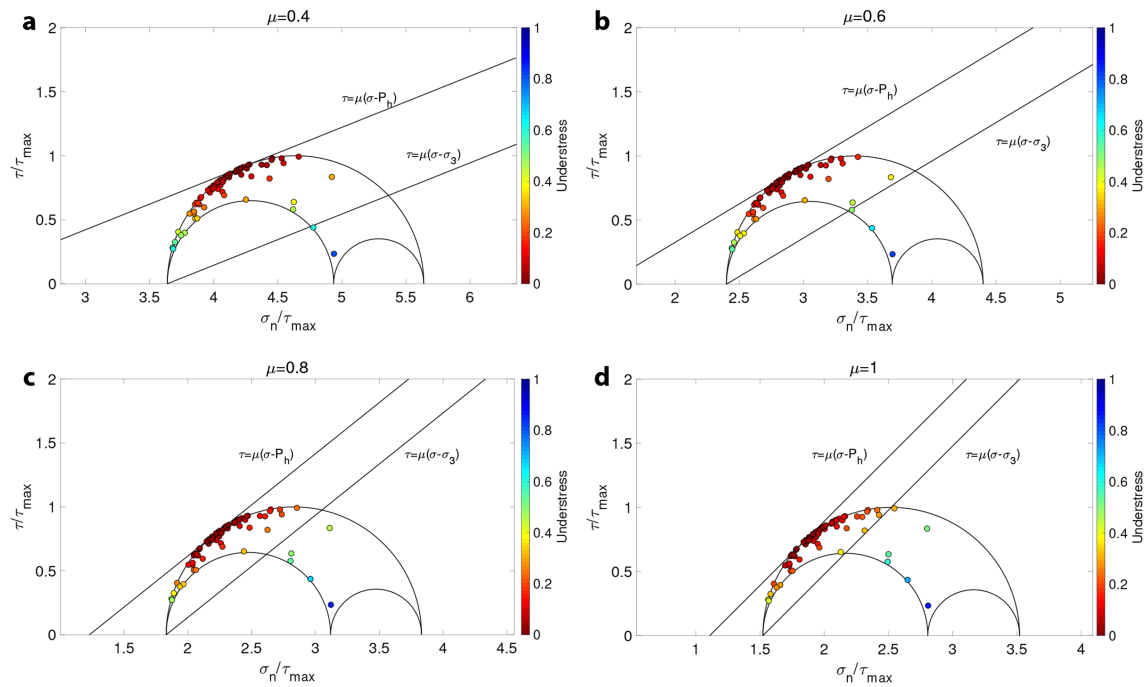


Figure 6. Dependence of the fault stress state on friction coefficients of 0.4, 0.6, 0.8, and 1.0. The plot schemes are the same as in Figure 3.

5.2. Stress Tensor Heterogeneity

In the analysis above, we use a stress tensor with a spatially uniform amplitude and the local stress orientations for each grid to calculate the understress parameter of the nearby faults. The uniform stress amplitude is taken as the mean value of the calculated absolute principal stress of all grids. To examine the validity of the uniform amplitude measure, we compare the fault stress state based on three different stress field maps: (1) a stress field with uniform stress amplitude (the average stress amplitudes above) and uniform stress orientations with horizontal $N85^\circ E$ σ_1 and vertical σ_2 in a strike-slip faulting regime; (2) a stress field with a uniform stress amplitude and local stress orientations, which is used in the analysis of this study; and (3) a stress field with local stress amplitudes and local stress orientations for each grid. Under each scenario, we calculate the understress parameter of each fault and show them in Figure 5.

The main difference between Scenarios 1 and 2 is the spatial variation of principal stress orientations. Results from Scenario 1 for some seismogenic faults are consistent with previous studies: for example, the Prague fault is optimally oriented with understress ~ 0.002 , consistent with Marsh and Holland (2016). However, the understress parameter shows differences with local stress orientations considered in Scenario 2. Compared to Scenario 2, the criticality of the faults in Scenario 1 can be either overestimated or underestimated, where 14% of the seismogenic faults have understress changes exceeding 0.1 (Figures 5a and 5b). The difference between two scenarios suggests that the heterogeneity of stress orientations has important implications on the inferred fault stress state.

We further consider the variability of stress amplitude by comparing results from Scenarios 2 and 3 in Figures 5c and 5d. In contrast to the large difference between Scenarios 1 and 2, the difference between 2 and 3 is smaller, with only one fault having an understress difference larger than 0.1. This result suggests that the local principal stress orientations have a more significant effect on fault stress state than do the stress amplitudes and that assuming a uniform stress amplitude does not significantly affect the results.

5.3. Effect of the Friction Coefficient

The fault orientation analysis in this study is based on the assumption of constant coefficient of friction of 0.68. Using a uniform friction coefficient for the whole study area, we attribute the fault strength heterogeneity to the variations of fluid pore pressure acting on the fault. The assumption is in part supported by the findings from laboratory experiments on Oklahoma basement rock (Kolawole, Johnston, et al., 2019) and in situ stress measurement in deep boreholes that the heterogeneity of friction coefficients within different rock types is substantially smaller than the fluid pore pressure heterogeneity (Terakawa et al., 2012).

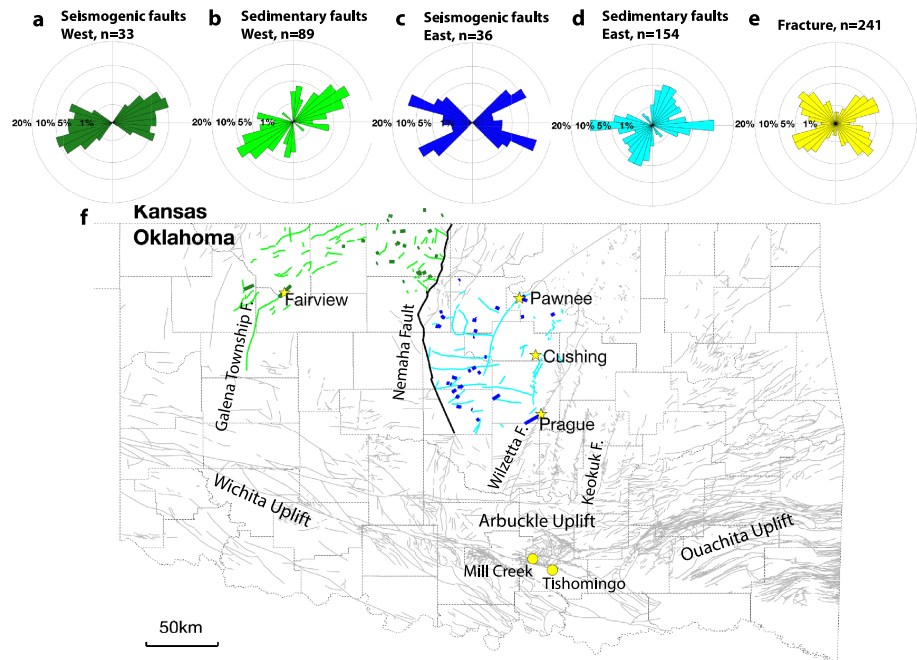


Figure 7. Strike comparisons of different categories of faults. (a) Seismogenic faults in the western pressurized section. (b) Mapped sedimentary fault in the western section. (c) Seismogenic faults in the eastern pressurized section. (d) Mapped sedimentary faults in the eastern section. (e) Mapped fractures in Mill Creek and Tishomingo, Oklahoma. The mapped sedimentary faults are from Marsh and Holland (2016). (f) The fault map with the same color scheme as the rose diagrams. The western and eastern pressurized sections are separated by the Nemaha Fault. Yellow dots denote the locations of exposed fractures. Some long N-S trending faults from Marsh and Holland (2016) are labeled, including the Nemaha Fault, Wilzetta Fault, Keokuk Fault, and the Galena Township Fault. The figure also labels the geological province in the south of Oklahoma (Northcutt & Campbell, 1969).

Without further knowledge of the spatial heterogeneity of the friction coefficients, we perform a sensitivity analysis where we vary the coefficient of friction, using constant values of 0.4, 0.6, 0.8, and 1.0 to calculate the stress tensor and understress parameter for seismogenic faults following the same process as for $\mu = 0.68$. The results are shown in Figure 6. This experiment demonstrates that the fault understress state is moderately sensitive to the assumed friction coefficient. If we define the optimally oriented faults as those with understress smaller than 0.2, friction coefficients of 0.4, 0.6, 0.8, and 1.0 will identify 72.46%, 76.81%, 75.36%, and 71.01% of seismogenic faults as optimally oriented faults, respectively, compared to 78.26% for $\mu = 0.68$. Under a friction coefficient of 0.68, we get the largest percentage of optimally oriented faults. It suggests that we have chosen a value close to the true friction coefficient in the study area. In the future studies, a better knowledge of the spatial distribution of friction coefficient will help further characterize the fault stress state.

5.4. Seimogenic Faults, Sedimentary Faults, and Their Common Tectonic Control

In this study, seimogenic faults are identified from lineaments of seismicity, so most of the faults are located in the crystalline basement. These faults show different orientations from mapped faults in OGS database (Marsh & Holland, 2016), which is compiled from past literature and data contributed by the oil and gas industry. They are primarily faults in the sedimentary sequences and are referred to as sedimentary faults. Considering that Nemaha fault acts as a pressure boundary in hydrologic modeling, we separate north-central Oklahoma into east and west sections and compare the fault orientations in each section (Figure 7). In the west section, the seimogenic faults (Figure 7a) show patterns of $[55^\circ, 75^\circ]$ and $[105^\circ, 125^\circ]$, and the sedimentary faults (Figure 7b) show a dominant trend of $[45^\circ, 75^\circ]$ and a minor trend of $[0^\circ, 10^\circ]$. For both types of faults, the NE trending set is more prominent than the NW trending set. It is possibly related to an overwhelming dominance of NE trending basement-rooted splays (synthetic Reidels; Liao et al., 2017; Curren & Bird, 2014) distributed along a few large N-S trending basement faults, for example, the Galena Township Fault.

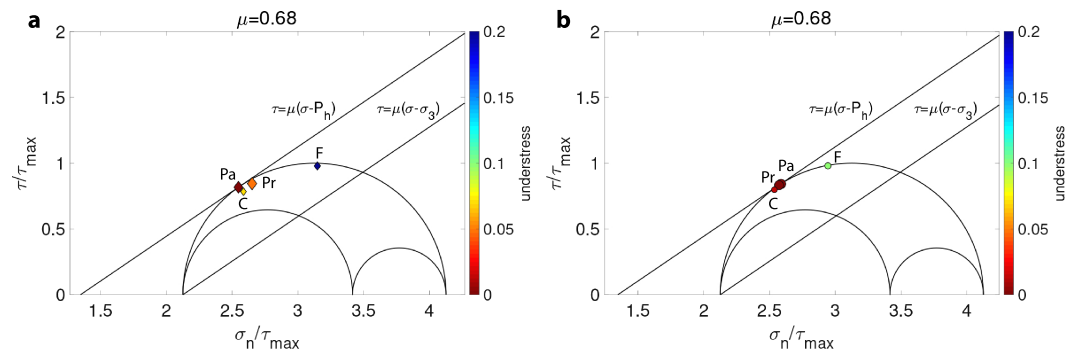


Figure 8. Understress for (a) the focal mechanism solutions of $M \geq 5.0$ mainshocks and (b) the hosting seismogenic faults as listed in Table S1. Diamonds: focal mechanism solutions. Circles: seismogenic faults. Both symbols are colored by understress values and scaled with the magnitude of the mainshock. Pr = Prague; Pa = Pawnee; C = Cushing; F = Fairview.

In the east section, the seismogenic faults (Figure 7c) show excellent correspondence with the observations of basement faults on 3-D seismic data in northeast Oklahoma (Kolawole, Johnston, et al., 2019). Both the NE and NW trends are reactivated in the current stress field. The sedimentary faults show dominant trends of NNE to NE, and E-W Figure 7d, which are possibly associated with the large basement-rooted NNE faults. The sedimentary faults are poorly oriented in the present-day stress field and do not have earthquakes associated with them currently. Although the NW and NE trends are the most reactivated trends associated with earthquakes, the E-W trend could still pose an important seismic hazard. Localized stress perturbation of the E-W trending faults in the area results in their seismogenic reactivation as observed within the Jones swarm (Holland, 2013).

In addition to the seismogenic faults and sedimentary faults in north-central Oklahoma, we also include measurements of exposed granite fractures from Mill Creek and Tishomingo in southern Oklahoma. The fractures are mapped at the satellite-scale from Google Earth images with a spatial resolution of 15 m. The basement fractures (Figure 7e) exhibit similar conjugate patterns as the seismogenic faults and are also consistent with the measurements of Precambrian basement fabrics in Kolawole, Johnston, et al. (2019). Although our comparison of the seismogenic faults with previously mapped sedimentary faults and Precambrian basement fabric likely reveal a common tectonic control, we observe spatial variations in the azimuth of the reactivated fault systems. This variation of reactivated trends may be controlled by both the relative abundance of the basement-rooted fault trends (emplaced by past tectonic events) and the variation of the local stress field across the eastern and western sections of the Oklahoma seismic zone, which might have been influenced by the Nemaha uplift structure.

5.5. Faults With $M \geq 5.0$ Earthquakes

Since 2011, four large earthquakes ($M \geq 5.0$) have occurred in Oklahoma: the M5.7 Prague earthquake in 2011, and the M5.1 Fairview, M5.8 Pawnee, and M5.0 Cushing earthquakes in 2016. None of these earthquakes occurred along previously mapped faults (e.g., Chen et al., 2017; Yeck et al., 2017). The geometries of the seismogenic faults delineated from seismicity are mostly consistent with the focal mechanism solutions of the mainshocks (Table S1). With an in situ stress field, we calculate the stress state of the mainshock fault planes from focal mechanism solutions and the corresponding seismogenic faults with the assumption of a constant friction coefficient of $\mu = 0.68$. As shown in Figure 8, the faults that hosted the M5.7 Prague, M5.8 Pawnee, and M5.0 Cushing earthquakes have understress smaller than 0.02, suggesting the faults in Prague, Pawnee, and Cushing were critically stressed and failed under a small perturbation of pore pressure. The seismogenic fault in Fairview is the least optimally oriented with an understress parameter of 0.1, and the fault plane of the mainshock has even higher understress of 0.2, which is likely due to the shallower dipping angle of 66° . Goebel et al. (2017) calculated poroelastic stress perturbations in the Fairview area from a group of high-rate injection wells to the northeast. Their results suggest that the poroelastic stress increase at the distance of the Fairview area is about 100 kPa and the fault orientation is about 15° off the optimal orientation that would receive maximum Coulomb stress change. Their results are consistent with the relatively high understress value obtained here for the Fairview fault. Figure 8 also shows that Fairview fault has highest relative shear stress compared to the other three faults, indicating highest frictional strength

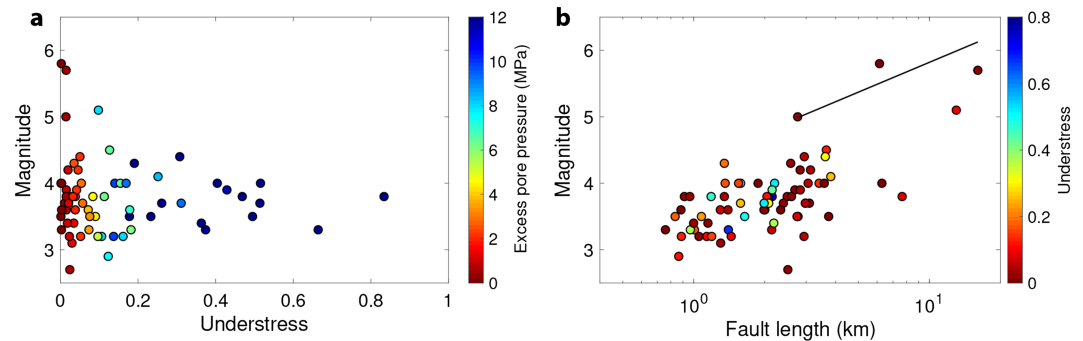


Figure 9. (a) Scatter plot of the maximum earthquake magnitude and understress value on each fault. The dots are colored by excess pore pressure. (b) Scatter plot of maximum earthquake magnitude and fault length. The dots are colored by understress value. The black line is the empirical relation between magnitude and rupture length from natural earthquakes: $M = 4.33 + 1.49 \log(\text{RLD}; M > 4.5)$, RLD = subsurface rupture length (km; Wells & Coppersmith, 1994).

(Yoshida et al., 2016). The relative frictional strength variations is qualitatively consistent with observations in Wu et al. (2018), where the Fairview fault has highest overall stress drop compared to the other fault zones, similar to the observations for a fluid induced earthquake swarm in Japan (Yoshida et al., 2017).

Gischig (2015) performed numerical modeling to investigate the effect of the fault orientation on rupture propagation, and the results suggest that optimally oriented faults tend to have uncontrolled ruptures that propagate beyond the pressure front, while less optimally oriented faults tend to have ruptures controlled by the extent of the pressurized zones. From this perspective, the understress parameter can provide insight into the fault rupture process, and hence the seismicity distribution for the M5 sequences. To the first order, the Prague, Pawnee, and Cushing sequences, which are on optimally oriented fault planes, are predominantly mainshock-aftershock sequences (Figure S9), with large values of skewness of moment release (Zhang & Shearer, 2016), while the Fairview sequence on the least optimally oriented fault is mainly a swarm-type sequence with an extended foreshock sequence leading up to the M5 earthquake resulting in the smallest skewness. Thus, our findings are at least consistent with a hypothesis that the fault criticality influences the temporal evolution of earthquake sequences.

5.6. Earthquake Hazard Potential

The maximum magnitude of induced earthquakes during and after injection is essential in evaluating seismic hazard. Several hypotheses have been proposed to understand the maximum magnitude as summarized in Eaton and Igonin (2018). McGarr (2014) proposed that the maximum magnitude can be constrained by the total injection volume and the area of the pressurized zone, which is consistent with the modeling results in Dieterich et al. (2015). In contrast, van der Elst et al. (2016) proposed that the maximum magnitude is related to the magnitude-frequency distribution of the induced earthquake sequence and related to the b value and the seismogenic index model proposed by Shapiro et al. (2011). Both models are consistent with the observations. However, it is important to recognize that the fault stress state may have a strong influence on how a rupture grows along the fault. The possibility that quasi-static slip along a pressurized fault grows into dynamic slip beyond the pressurized area has been demonstrated theoretically by Garagash and Germanovich (2012) and verified by a stochastic model in Gischig and Wiemer (2013).

The fault length provides a direct measurement to estimate the maximum magnitude. Both fault orientation and fault length can influence the maximum magnitude of induced earthquakes. In Figure 9a, we plot the maximum earthquake magnitude and fault understress state. For optimally oriented faults (understress < 0.2), the fault has a broader range of magnitudes observed. For nonoptimally oriented faults, there are no earthquakes larger than magnitude 4.5. Intermediate to small earthquakes ($M < 4.0$) occurred on both critically stressed and noncritically stressed faults with a relatively low shear stress, which could be attributed to increased pore pressure. We map 54 optimally oriented faults and 15 nonoptimally oriented faults. It is still possible that large earthquakes have the same probability to occur on nonoptimally oriented faults, and the lack of large earthquakes on nonoptimally oriented faults is due to its low abundance (Table S2).

Figure 9b shows that the maximum magnitude on the faults increases with the fault length. The largest earthquakes (Prague, Pawnee, and Cushing earthquakes) occurred on critically stressed faults, and the magnitudes are comparable to the predicted values from the empirical relationship for natural earthquakes (Wells & Coppersmith, 1994), indicating that the largest earthquakes might be controlled by the local stress field. To examine the alternative possibility that large earthquakes control apparent fault size, we plot the seismicity prior and after the mainshock in four M5 clusters (Figure S10). The results show that the events before the mainshock already spread over the whole length of the fault in Fairview, Pawnee, and Cushing, which suggests that the fault length is not controlled by the mainshock and its aftershocks. Similar observations have been found by Schoenball and Ellsworth (2017b). In Prague, it seems that the fault length is controlled by the mainshock (aftershocks). However, due to the lack of stations at that time, it is also possible that some events before mainshock are missing in the catalog. Based on current data, we cannot draw an unambiguous relationship between understress and maximum magnitude. However, the knowledge of fault stress state can help identify high-risk faults with potential runaway ruptures and large earthquakes (Galis et al., 2017).

6. Conclusions

To better characterize the properties and stress state of fault systems in Oklahoma and southern Kansas, we map the fault geometry using high-precision earthquake relocations and generate a high-resolution in situ stress map using focal mechanism solutions. Our results suggest the following:

1. Although the majority of the seismogenic faults (NE and NW trending) are optimally oriented relative to the local stress field, some nonoptimally oriented faults are identified.
2. Comparison of the seismogenic faults with sedimentary faults and mapped basement fractures suggests potentially similar tectonic origins for those structures.
3. The orientations of the faults that hosted the largest earthquakes ($M \geq 5.0$) in Oklahoma are quantitatively characterized, and the Prague, Pawnee, and Cushing faults are optimally oriented faults, while the Fairview fault is not. For the three optimally oriented faults, the maximum earthquake magnitudes are comparable to the predictions from the empirical scaling relation for natural earthquakes, and the three sequences are predominately mainshock-aftershock type sequences.

Our study contributes detailed seismogenic fault analysis to the current fault database and provides a more complete picture of the relation among seismogenic fault properties, pore pressure, the local stress field, and rupture process in the region of induced seismicity.

References

- Alt, R. C., & Zoback, M. D. (2017). In situ stress and active faulting in Oklahoma. *Bulletin of the Seismological Society of America*, *107*(1), 216–228. <https://doi.org/10.1785/0120160156>
- Altmann, J., Müller, B., Müller, T., Heidbach, O., Tingay, M., & Weißhardt, A. (2014). Pore pressure stress coupling in 3D and consequences for reservoir stress states and fault reactivation. *Geothermics*, *52*, 195–205. <https://doi.org/10.1016/j.geothermics.2014.01.004>
- Barbour, A. J., Norbeck, J. H., & Rubinstein, J. L. (2017). The effects of varying injection rates in Osage County, Oklahoma, on the 2016 M_w 5.8 Pawnee earthquake. *Seismological Research Letters*, *88*(4), 1040–1053.
- Bickford, M., Van Schmus, W., Karlstrom, K., Mueller, P., & Kamenov, G. (2015). Mesoproterozoic-trans-Laurentian magmatism: A synthesis of continent-wide age distributions, new SIMS U–Pb ages, zircon saturation temperatures, and Hf and Nd isotopic compositions. *Precambrian Research*, *265*, 286–312.
- Bott, M. H. P. (1959). The mechanics of oblique slip faulting. *Geological Magazine*, *96*(2), 109–117. <https://doi.org/10.1017/S0016756800059987>
- Byerlee, J. (1978). Friction of rocks. *Pure and Applied Geophysics PAGEOPH*, *116*(4–5), 615–626. <https://doi.org/10.1007/BF00876528>
- Cappa, F., Scuderi, M. M., Colletini, C., Guglielmi, Y., & Avouac, J.-P. (2019). Stabilization of fault slip by fluid injection in the laboratory and in situ. *Science Advances*, *5*(3), eaau4065. <https://doi.org/10.1126/sciadv.aau4065>
- Chen, C. (2016). Comprehensive analysis of Oklahoma earthquakes: From earthquake monitoring to 3-D tomography and relocation, University of Oklahoma, PhD thesis.
- Chen, X., Haffener, J., Goebel, T. H., Meng, X., Peng, Z., & Chang, J. C. (2018). Temporal correlation between seismic moment and injection volume for an induced earthquake sequence in central Oklahoma. *Journal of Geophysical Research: Solid Earth*, *123*, 3047–3064. <https://doi.org/10.1002/2017JB014694>
- Chen, X., Nakata, N., Pennington, C., Haffener, J., Chang, J. C., He, X., et al. (2017). The Pawnee earthquake as a result of the interplay among injection, faults and foreshocks. *Scientific Reports*, *7*(1), 1–18. <https://doi.org/10.1038/s41598-017-04992-z>
- Chopra, S., Kurt, M., Folarin, K., & Brett, M. C. (2018). Nemaha strike-slip fault expression on 3-D seismic data in scoop trend. AAPG Explorer.
- Curran, I. S., & Bird, P. (2014). Formation and suppression of strike-slip fault systems. *Pure and Applied Geophysics*, *171*(11), 2899–2918.
- Darold, A., & Holland, A. (2015). Preliminary Oklahoma optimal fault orientations. Oklahoma Geol. Surv. Open File Rep., OF4.

Acknowledgments

This work was supported by the Oklahoma Governor's Emergency Funding for Induced Seismicity, USGS NEHRP external research grant G18AP00022, and graduate student fellowship at the School of Geosciences at the University of Oklahoma. D. Trugman acknowledges institutional support from the Laboratory Directed Research and Development (LDRD) program of Los Alamos National Laboratory under project number 20180700PRD1. We thank the personnel at the Oklahoma Geological Survey (OGS) for sharing focal mechanism and fault data. Focal mechanism data used in this study are included as Data Sets S1 and S2 and available by requesting them from OGS. Fault data are available online (at <http://www.ou.edu/ogs/data/fault>). We thank the Oklahoma Corporation Commission and the Kansas Corporation Commission for providing wastewater disposal data. We also thank Candace Johnston for data regarding surface fracture orientations in south-central Oklahoma. Finally, we are grateful for the constructive comments of two anonymous reviewers and the editors, whose suggestions improved the quality and clarity of the manuscript.

- Deng, K., Liu, Y., & Harrington, R. M. (2016). Poroelastic stress triggering of the December 2013 Crooked Lake, Alberta, induced seismicity sequence. *Geophysical Research Letters*, *43*, 8482–8491. <https://doi.org/10.1002/2016GL070421>
- Denison, R. E., Bickford, M., Lidiak, E. G., & Kisvarsanyi, E. (1987). Geology and geochronology of precambrian rocks in the central interior region of the united states.
- Dieterich, J. H., Richards-dinger, K. B., & Kroll, K. A. (2015). Modeling injection-induced seismicity with the physics-based earthquake simulator RSQSim. *Seismological Research Letters*, *86*(4), 1102–1109. <https://doi.org/10.1785/0220150057>
- Eaton, D. W., & Igonin, N. (2018). What controls the maximum magnitude of injection-induced earthquakes? *The Leading Edge*, *37*(2), 135–140. <https://doi.org/10.1190/tle37020135.1>
- Ellsworth, W. L. (2013). Injection-induced Earthquakes. *Science*, *341*(6142), 1225–1229. <https://doi.org/10.1126/science.1225942>
- Eyre, T. S., Eaton, D. W., Garagash, D. I., Zecevic, M., Venieri, M., Weir, R., & Lawton, D. C. (2019). The role of aseismic slip in hydraulic fracturing-induced seismicity. *Science Advances*, *5*(8), eaav7172. <https://doi.org/10.1126/sciadv.aav7172>
- Galis, M., Ampuero, J. P., Mai, P. M., & Cappa, F. (2017). Induced seismicity provides insight into why earthquake ruptures stop. *Science Advances*, *3*(12), eaap7528. <https://doi.org/10.1126/sciadv.aap7528>
- Garagash, D. I., & Germanovich, L. N. (2012). Nucleation and arrest of dynamic slip on a pressurized fault. *Journal of Geophysical Research: Solid Earth*, *117*, B10310. <https://doi.org/10.1029/2012JB009209>
- Gischig, V. S. (2015). Rupture propagation behavior and the largest possible earthquake induced by fluid injection into deep reservoirs. *Geophysical Research Letters*, *42*, 7420–7428. <https://doi.org/10.1002/2015GL065072>
- Gischig, V. S., & Wiemer, S. (2013). A stochastic model for induced seismicity based on non-linear pressure diffusion and irreversible permeability enhancement. *Geophysical Journal International*, *194*(2), 1229–1249. <https://doi.org/10.1093/gji/ggt164>
- Goebel, T. H., Weingarten, M., Chen, X., Haffener, J., & Brodsky, E. E. (2017). The 2016 Mw5.1 Fairview, Oklahoma earthquakes: Evidence for long-range poroelastic triggering at >40 km from fluid disposal wells. *Earth and Planetary Science Letters*, *472*, 50–61. <https://doi.org/10.1016/j.epsl.2017.05.011>
- Haffener, J., Chen, X., & Murray, K. (2018). Multiscale analysis of spatiotemporal relationship between injection and seismicity in Oklahoma. *Journal of Geophysical Research: Solid Earth*, *123*, 8711–8731. <https://doi.org/10.1029/2018JB015512>
- Hardebeck, J. L., & Hauksson, E. (2001). Crustal stress field in southern California and its implications for fault mechanics. *Journal of Geophysical Research*, *106*(B10), 21,859–21,882.
- Hardebeck, J. L., & Michael, A. J. (2006). Damped regional-scale stress inversions: Methodology and examples for southern California and the Coalinga aftershock sequence. *Journal of Geophysical Research*, *111*, B11310. <https://doi.org/10.1029/2005JB004144>
- Hardebeck, J. L., & Shearer, P. M. (2008). *Hash: A fortran program for computing earthquake first-motion focal mechanisms-v1. 2-january*, *31*, 1–17.
- Healy, J., Rubey, W., Griggs, D., & Raleigh, C. (1968). The Denver earthquakes. *Science*, *161*(3848), 1301–1310. <https://doi.org/10.1126/science.161.3848.1301>
- Holland, A. A. (2013). Optimal fault orientations within Oklahoma. *Seismological Research Letters*, *84*(5), 876–890. <https://doi.org/10.1785/0220120153>
- Keranen, K. M., Savage, H. M., Abers, G. A., & Cochran, E. S. (2013). Potentially induced earthquakes in Oklahoma, USA: Links between wastewater injection and the 2011 Mw 5.7 earthquake sequence. *Geology*, *41*(6), 699–702. <https://doi.org/10.1130/G34045.1>
- Keranen, K. M., Weingarten, M., Abers, G. A., Bekins, B. A., & Ge, S. (2014). Sharp increase in central Oklahoma seismicity since 2008 induced by massive wastewater injection. *Science*, *345*(6195), 448–451. <https://doi.org/10.1126/science.1255802>
- King Hubbert, M., & Rubey, W. W. (1959). Role of fluid pressure in mechanics of overthrust faulting: I. Mechanics of fluid-filled porous solids and its application to overthrust faulting. *Bulletin of the Geological Society of America*, *70*(2), 115–166. [https://doi.org/10.1130/0016-7606\(1959\)70\[115:ROFPIM\]2.0.CO;2](https://doi.org/10.1130/0016-7606(1959)70[115:ROFPIM]2.0.CO;2)
- Kolawole, F., Carpenter, B., Reches, Z., & Simpson, M. T. (2019). Basement-driven deformation of the sedimentary sequence in north-central Oklahoma. In *2019 AAPG Annual Convention and Exhibition*. San Antonio, Texas. <https://www.searchanddiscovery.com/abstracts/html/2019/ace2019/abstracts/2010.html>
- Kolawole, F., Johnston, C. S., Morgan, C. B., Chang, J. C., Marfurt, K. J., Lockner, D. A., et al. (2019). *The susceptibility of Oklahoma's basement to seismic reactivation* (Vol. 12, pp. 839–844). <https://doi.org/10.1038/s41561-019-0440-5>
- Langenbruch, C., Weingarten, M., & Zoback, M. D. (2018). Physics-based forecasting of man-made earthquake hazards in Oklahoma and Kansas. *Nature Communications*, *9*(1), 3946. <https://doi.org/10.1038/s41467-018-06167-4>
- Levandowski, W., Herrmann, R. B., Briggs, R., Boyd, O., & Gold, R. (2018b). An updated stress map of the continental United States reveals heterogeneous intraplate stress. *Nature Geoscience*, *11*. <https://doi.org/10.1038/s41561-018-0120-x>
- Levandowski, W., Weingarten, M., & Walsh, R. III (2018a). Geomechanical sensitivities of injection-induced earthquakes. *Geophysical Research Letters*, *45*, 8958–8965. <https://doi.org/10.1029/2018GL077551>
- Liao, Z., Liu, H., Jiang, Z., Marfurt, K. J., & Reches, Z. (2017). Fault damage zone at subsurface: A case study using 3D seismic attributes and a clay model analog for the Anadarko basin, Oklahoma. *Interpretation*, *5*(2), T143–T150. <https://doi.org/10.1190/INT-2016-0033.1>
- Marsh, S., & Holland, A. (2016). Comprehensive fault database and interpretive fault map of Oklahoma (*Geol Surv. Open-File Rept. OF2-2016*). Norman, OK: Oklahoma Geological Survey. p. 15.
- Martínez-Garzón, P., Ben-Zion, Y., Abolfathian, N., Kwiatek, G., & Bohnhoff, M. (2016a). A refined methodology for stress inversions of earthquake focal mechanisms. *Journal of Geophysical Research: Solid Earth*, *121*, 8666–8687. <https://doi.org/10.1002/2016JB013493>
- Martínez-Garzón, P., Bohnhoff, M., Kwiatek, G., & Dresen, G. (2013). Stress tensor changes related to fluid injection at the Geysers Geothermal Field, California. *Geophysical Research Letters*, *40*, 2596–2601. <https://doi.org/10.1002/grl.50438>
- Martínez-Garzón, P., Kwiatek, G., Bohnhoff, M., & Dresen, G. (2016c). Impact of fluid injection on fracture reactivation at the Geysers Geothermal Field. *Journal of Geophysical Research: Solid Earth*, *121*, 7432–7449. <https://doi.org/10.1002/2016JB013137>
- Martínez-Garzón, P., Kwiatek, G., Ickrath, M., & Bohnhoff, M. (2014). MSATSI: A MATLAB package for stress inversion combining solid classic methodology, a new simplified User-Handling, and a visualization tool. *Seismological Research Letters*, *85*(4), 896–904. <https://doi.org/10.1785/0220130189>
- Martínez-Garzón, P., Vavryčuk, V., Kwiatek, G., & Bohnhoff, M. (2016b). Sensitivity of stress inversion of focal mechanisms to pore pressure changes. *Geophysical Research Letters*, *43*, 8441–8450. <https://doi.org/10.1002/2016GL070145>
- McGarr, A. (2014). Maximum magnitude earthquakes induced by fluid injection. *Journal of Geophysical Research: Solid Earth*, *119*, 1008–1019. <https://doi.org/10.1002/2013JB010597>
- Michael, A. J. (1984). Determination of stress from slip data: Faults and folds. *Journal of Geophysical Research*, *89*(B13), 11,517–11,526. <https://doi.org/10.1029/JB089iB13p11517>
- Northcutt, R. A., & Campbell, J. A. (1969). Geologic provinces of Oklahoma. pp. 128–134.
- Qi, W. (2016). Stress analysis of recent earthquakes in Oklahoma (Master's thesis), University of Oklahoma.

- Quinones, L. A., DeShon, H. R., Magnani, M. B., & Frohlich, C. (2018). Stress orientations in the fort worth basin, texas, determined from earthquake focal mechanisms stress orientations in the fort worth basin. *Bulletin of the Seismological Society of America*, *108*(3A), 1124. <https://doi.org/10.1785/0120170337>
- Raleigh, C. B., Healy, J. H., & Bredehoeft, J. D. (1976). An experiment in earthquake control at Rangely, Colorado. *Science*, *191*(4233), 1230–1237. <https://doi.org/10.1126/science.191.4233.1230>
- Rubinstein, J. L., Ellsworth, W. L., & Dougherty, S. L. (2018). The 2013–2016 induced earthquakes in harper and Sumner counties, southern Kansas. *Bulletin of the Seismological Society of America*, *108*(2), 674–689. <https://doi.org/10.1785/0120170209>
- Schoenball, M., & Ellsworth, W. L. (2017a). Waveform-relocated earthquake catalog for Oklahoma and southern Kansas illuminates the regional fault network. *Seismological Research Letters*, *88*, 1252–1258. <https://doi.org/10.1785/0220170083>
- Schoenball, M., & Ellsworth, W. L. (2017b). A systematic assessment of the spatiotemporal evolution of fault activation through induced seismicity in Oklahoma and southern Kansas. *Journal of Geophysical Research: Solid Earth*, *122*, 10,189–10,206. <https://doi.org/10.1002/2017JB014850>
- Segall, P., & Lu, S. (2015). Injection-induced seismicity: Poroelastic and earthquake nucleation effects. *Journal of Geophysical Research: Solid Earth*, *120*, 5082–5103. <https://doi.org/10.1002/2015JB012060>
- Shapiro, S. A., Krüger, O. S., Dinske, C., & Langenbruch, C. (2011). Magnitudes of induced earthquakes and geometric scales of fluid-stimulated rock volumes. *Geophysics*, *76*(6), WC55–WC63. <https://doi.org/10.1190/geo2010-0349.1>
- Skoumal, R. J., Kaven, J. O., & Walter, J. I. (2019). *Characterizing seismogenic fault structures in Oklahoma using a relocated template-matched catalog* (Vol. 90, pp. 1535–1543). <https://doi.org/10.1785/0220190045>
- Snee, J.-E. L., & Zoback, M. D. (2016). State of stress in texas: Implications for induced seismicity. *Geophysical Research Letters*, *43*, 10,208–10,214. <https://doi.org/10.1002/2016GL070974>
- Terakawa, T., Miller, S. A., & Deichmann, N. (2012). High fluid pressure and triggered earthquakes in the enhanced geothermal system in Basel, Switzerland. *Journal of Geophysical Research*, *117*, B07305. <https://doi.org/10.1029/2011JB008980>
- Terakawa, T., Zoprowski, A., Galvan, B., & Miller, S. A. (2010). High-pressure fluid at hypocentral depths in the L'Aquila region inferred from earthquake focal mechanisms. *Geology*, *38*(11), 995–998. <https://doi.org/10.1130/G31457.1>
- van der Elst, N. J., Page, M. T., Weiser, D. A., Goebel, T. H., & Hosseini, S. M. (2016). Induced earthquake magnitudes are as large as (statistically) expected. *Journal of Geophysical Research: Solid Earth*, *121*, 4575–4590. <https://doi.org/10.1002/2016JB012818>
- Vavryčuk, V. (2014). Iterative joint inversion for stress and fault orientations from focal mechanisms. *Geophysical Journal International*, *199*(1), 69–77. <https://doi.org/10.1093/gji/ggu224>
- Vidale, J. E., & Shearer, P. M. (2006). A survey of 71 earthquake bursts across southern California: Exploring the role of pore fluid pressure fluctuations and aseismic slip as drivers. *Journal of Geophysical Research*, *111*, B05312. <https://doi.org/10.1029/2005JB004034>
- Waldhauser, F. (2001). Hypod—A program to compute double-difference hypocenter locations (hypoDD Version 1.0-03/2001) (*US Geol. Surv. Open File Rep.*, 01, 113). Menlo Park, CA.
- Wallace, R. E. (1951). Geometry of shearing stress and relation to faulting. *The Journal of Geology*, *59*(2), 118–130. <https://doi.org/10.1086/625831>
- Walsh, F. R., & Zoback, M. D. (2016). Probabilistic assessment of potential fault slip related to injection-induced earthquakes: Application to north-central Oklahoma, USA. *Geology*, *44*(12), 991–994. <https://doi.org/10.1130/G38275.1>
- Sylvester, A. G. (1988). Strike-slip faults. *Bulletin of Geological Society of America*, *100*(11), 1666–1703. [http://doi.org/10.1130/0016-7606\(1988\)100<1666:SSF>2.3.CO;2](http://doi.org/10.1130/0016-7606(1988)100<1666:SSF>2.3.CO;2)
- Wells, D. L., & Coppersmith, K. J. (1994). New empirical relationships among magnitude, rupture length, rupture width, rupture area, and surface displacement. *Bulletin of the Seismological Society of America*, *84*(4), 974–1002.
- Whitmeyer, S. J., & Karlstrom, K. E. (2007). Tectonic model for the proterozoic growth of north america. *Geosphere*, *3*(4), 220–259.
- Wu, Q., Chapman, M., & Chen, X. (2018). Stress-drop variations of induced earthquakes in Oklahoma. *Bulletin of the Seismological Society of America*, *108*(3A), 1107–1123. <https://doi.org/10.1785/0120170335>
- Yeck, W. L., Hayes, G. P., McNamara, D. E., Rubinstein, J. L., Barnhart, W. D., Earle, P. S., & Benz, H. M. (2017). Oklahoma experiences largest earthquake during ongoing regional wastewater injection hazard mitigation efforts. *Geophysical Research Letters*, *44*, 711–717. <https://doi.org/10.1002/2016GL071685>
- Yeck, W., Weingarten, M., Benz, H. M., McNamara, D. E., Bergman, E., Herrmann, R., et al. (2016). Far-field pressurization likely caused one of the largest injection induced earthquakes by reactivating a large preexisting basement fault structure. *Geophysical Research Letters*, *43*, 10,198–10,207. <https://doi.org/10.1002/2016GL070861>
- Yoshida, K., Hasegawa, A., & Yoshida, T. (2016). Temporal variation of frictional strength in an earthquake swarm in NE Japan caused by fluid migration. *Journal of Geophysical Research: Solid Earth*, *121*, 5953–5965. <https://doi.org/10.1002/2016JB013022>
- Yoshida, K., Saito, T., Urata, Y., Asano, Y., & Hasegawa, A. (2017). Temporal changes in stress drop, frictional strength, and earthquake size distribution in the 2011 Yamagata-Fukushima, NE Japan, earthquake swarm, caused by fluid migration. *Journal of Geophysical Research: Solid Earth*, *122*, 10–379. <https://doi.org/10.1002/2017JB014334>
- Zhang, Q., & Shearer, P. M. (2016). A new method to identify earthquake swarms applied to seismicity near the San Jacinto fault, California. *Geophysical Journal International*, *205*, 995–1005. <https://doi.org/10.1093/gji/ggw073>
- Zoback, M. L. (1992). First-and second-order patterns of stress in the lithosphere: The world stress map project. *Journal of Geophysical Research*, *97*(B8), 11,703–11,728. <https://doi.org/10.1029/92JB00132>